Plasmon-Enhanced Photoluminescence of Silicon Quantum Dots: Simulation and Experiment

Julie S. Biteen,[†] Luke A. Sweatlock,[†] Hans Mertens,[‡] Nathan S. Lewis,[†] Albert Polman,[‡] and Harry A. Atwater*[,†]

California Institute of Technology, Pasadena, California 91125, and Center for Nanophotonics, FOM-Institute AMOLF, Kruislaan 407, 1098 SJ Amsterdam, The Netherlands

Received: May 30, 2007; In Final Form: July 12, 2007

The enhancement of photoluminescence emission from silicon quantum dots in the near field of cylindrical silver particles has been calculated using finite integration techniques. This computational method permitted a quantitative examination of the plasmon resonance frequencies and locally enhanced fields surrounding coupled arrays of silver particles having arbitrary shapes and finite sizes. We have studied Ag nanoparticles with diameters in the 50−300 nanometer range and array pitches in the range of 50−800 nm, near a plane of optical emitters spaced 10−40 nm from the arrays. The calculated and experimental plasmon resonance frequencies and luminescence enhancements are in good agreement. In the tens-of-nanometers size regime, for the geometries under investigation, two competing factors affect the photoluminescence enhancement; on one hand, larger field enhancements, which produce greater emission enhancements, exist around smaller silver particles. However, as the spacing of such particles is decreased to attain higher surface coverages, the interparticle coupling draws the enhanced field into the lateral gaps between particles and away from the emitters, leading to a decrease in the plasmonic emission enhancement. The computations have thus revealed the limitations of using arbitrarily dense arrays of plasmonic metal particles to enhance the emission from coplanar arrays of dipole-like emitters. For such a geometry, a maximum sixfold net emission enhancement is predicted for the situation in which the plasmonic layer is composed of 50 nm diameter Ag particles in an array having a 300 nm pitch.

Introduction

Si quantum dots are of interest in potential applications ranging from biological sensing to light-emitting devices because the optoelectronic properties of zero-dimensional quantum dot silicon nanocrystals are different from the optical properties of bulk Si. In contrast to the very weak emission from bulk Si, silicon nanocrystals (nc-Si) having dimensions below ∼5 nm emit light efficiently and exhibit emission energies that can be tuned throughout the visible spectrum by varying the size of the nc-Si.[1−3] One important advantage of using light emitters based on silicon is that such systems can be fabricated with CMOS-compatible methods such as ion implantation.

The overall brightness of nc-Si is limited by the low emission decay rate, $10^4-10^5\ s^{-1}$, that results from the indirect band gap of silicon.[2] Plasmonic interactions, which exploit the intense local field near the surface of a metal particle or a rough metal surface, can modify the radiative decay rate and quantum efficiency and thus modify the photoluminescence (PL) intensity of an emitter.[4−6] The coupling of dyes and semiconductor quantum dots to the plasmon modes of silver and gold nanostructures has been shown to produce increased emission due to a plasmon-enhanced PL process.[7−10] This approach has been extended to control the PL intensity, radiative rate, and optical polarization properties of nc-Si,[11,12] and the observed PL enhancement for nc-Si has been shown to arise from a resonant interaction.[13] Measurements to date of the plasmon-enhanced PL of nc-Si have, however, been performed via far-field ensemble measurement techniques that do not provide spatially resolved information on the origin of the enhancement.[11−13] Thus, in addition to near-field interactions, other processes could possibly contribute to the observed PL enhancement in this system. A theoretical approach is therefore needed to distinguish between these effects.

Previous theoretical treatments used analytical approximations to investigate the properties of plasmon-enhanced emission with electrodynamical theory that provides exact results for spherical particles.[4−6] These models have recently been improved to include radiation damping and dynamic depolarization.[14] While the latter model can be generalized for spheroids, it cannot treat metal nanoparticles of arbitrary shape, nor can it account for interparticle coupling. In the present work, we are interested in quantitatively comparing calculated enhancements to experiments that involve arrays of nonspheroidal, coupled particles, and we desire to avoid the approximations required to perform an analytical analysis of such a system. Computational approaches, such as T-matrix solutions,[15] the discrete dipole approximation,[16−18] and finite-difference time-domain simulations,[19] have been utilized successfully in the past to examine the enhanced field about plasmonic metals. Given the lack of analytical models, we use a finite-element integration scheme of Maxwell's equations to calculate the resonance frequencies and mode intensity distributions for Ag particle arrays with arbitrary geometries in complex environments.

In this work, we have obtained quantitative information about the enhanced field experienced by silicon quantum dot emitters

* To whom correspondence should be addressed. E-mail: haa@caltech.edu.
[†] California Institute of Technology.
[‡] FOM-AMOLF.

10.1021/jp074160+ CCC: $37.00
Published on Web 08/17/2007

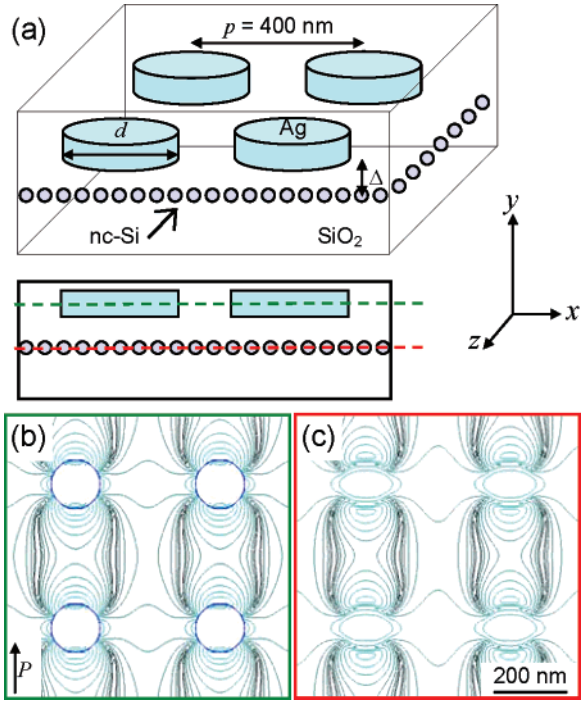

Figure 1. (a) Schematic of the simulated system showing a periodic array of Ag nanoparticles with pitch, p, and diameter, d, situated a distance, Δ, above a plane where Si quantum dots are located in the experimental configuration. Field intensity maps calculated for d = 135 nm, p = 400 nm, and λ_{exc} = 633 nm are plotted in the center plane of the np-Ag array (b) and in the plane 10 nm below the np-Ag (c). Four subsequent contour lines represent an order-of-magnitude change in the x-component of the field intensity. The arrow, P, in (b) indicates the polarization direction of the incident plane wave.

in the proximity of an array of lithographically defined silver particles. Full-field, finite-integration time-domain methods were used to simulate the frequency-dependent near-field and far-field optical properties of metal nanoparticle arrays. Specifically, the spectrum near the plasmon resonance has been simulated for planes of coupled, cylindrical np-Ag. Additionally, the enhancement of the local electric field intensity under the metal nanoparticle arrays has been calculated. The spatial distribution of nc-Si in the systems measured in ref 13 have been taken into account in our comparison between the calculated results and the experimental measurements. We have also calculated the influence of the diameter and interparticle spacing of the Ag nanoparticles on the resonant frequency and electric field enhancements. In addition to verifying the physics that underlie the experimental observations,[13] the electromagnetic simulations have been used to identify other, more optimal geometries that are predicted to exhibit larger field enhancements than the systems studied experimentally to date.

Field Enhancements and Spontaneous Emission. A formalism for evaluating the decay rate of optical emitters in the near-field of a metal nanostructure has been developed by Gersten and Nitzan.[4] The formalism has been extended by Wokaun et al. to include fully radiationless energy-transfer quenching[5] and has been more recently restated by Kümmerlen et al.[6] In the limit in which the calculated electric field distribution is dominated by dipole modes, the enhancement of the field intensity, $|E_{enh}|^2 / |E_0|^2$, is directly related to the photoluminescence radiative decay rate enhancement, $\Gamma_{rad,enh}$, that is[6]

$$\Gamma_{rad,enh}(\omega_{PL}) = \Gamma_{r,0}(\omega_{PL})|E_{enh}(\omega_{PL})|^2 / |E_0(\omega_{PL})|^2 \quad (1)$$

Computationally, the enhancement of the radiative decay rate of a dipole emitter in close proximity to a metal nanoparticle can be obtained by comparing the energy flux through a surface that encloses both the dipole source and the metal particle to the radiated power of the same dipole source in the metal of the particle.[20] Alternatively, by invoking the reciprocity theorem,[21] radiative decay rate modifications can be obtained from the enhancement, at the position of the emitter, of the electric field intensity generated by plane wave illumination. In general, this procedure requires averaging over all angles of incidence. However, for a particle that is much smaller than the wavelength of light, the electric field intensity generated by plane wave illumination is independent of the angle of incidence and depends only on polarization.[22] Consequently, finite-difference time-domain (FDTD) simulations of the electric field intensity generated by plane wave illumination from one specific angle can be used to obtain maps of the radiative decay rate enhancement near a small metal nanostructure. We adopt such an approach in the present paper and justify the approach in the Results and Discussion section.

Experimental Section

Three-dimensional full-field electromagnetic simulations using finite-difference integration techniques were performed to solve Maxwell's equations.[19] This method allowed simulations to be performed on the exact shape of the metal cylinders that were fabricated lithographically, with no need to approximate the cylinders as oblate ellipsoids, as is commonly done to facilitate the use of analytical calculations. The simulations accounted for retardation, nonradiative damping by Ohmic loss, and interparticle coupling.

The experimental samples of ref 13, to which the calculations were compared, consisted of 100 μm by 100 μm square arrays of cylindrical silver nanoparticles (np-Ag) that were 20 nm in height and had a range of diameters, d, between 135 and 320 nm. In the experiments, the nanoparticles were adhered, via a 2 nm thick amorphous Si wetting layer, onto the surface of a 3 mm thick substrate of fused silica doped with nc-Si at a depth of $\Delta \sim 10$ nm beneath the base of the np-Ag plane.

Computations were conducted on a system (Figure 1a) that, given the restrictions of the simulation package,[19] best emulated the experimental samples. The simulated np-Ag were cylinders 20 nm in height. The particle diameters in each array were chosen to correspond to those examined experimentally, based on scanning electron microscopy (SEM) data on the samples of interest.[13] A fixed pitch (particle center-to-center spacing) of p = 400 nm was considered in the simulations. The quasi-infinite arrays that were fabricated were simulated by using von Karman periodic boundary conditions to construct a two-dimensional infinite array of np-Ag. The simulation was performed over the volume of four particles that were arranged in a 300 nm deep, 800 nm by 800 nm box. This volume was divided into 2×10^5 grid cells that were refined to give the greatest detail in the area near the Ag particles. Simulations that have employed similar conditions have been shown previously to correspond well to experiments.[23]

The dielectric function of Ag, ϵ_{Ag}, as a function of radial frequency, ω, was approximated using a modified Drude model that was fitted to tabulated data over the wavelength range of interest[24]

$$\epsilon_{Ag}(\omega) = 5.45 - 0.73 \frac{\omega_{b,Ag}^2}{\omega^2 + i\omega\gamma_{Ag}} \quad (2)$$

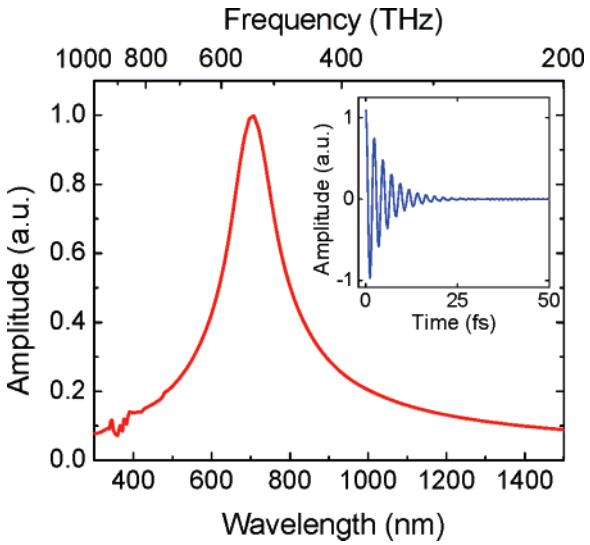

Figure 2. The np-Ag array plasmon resonance spectrum for a characteristic array ($d = 155$ nm, $p = 400$ nm), calculated via a Fourier transform of the electric field ring-down (shown in the inset).

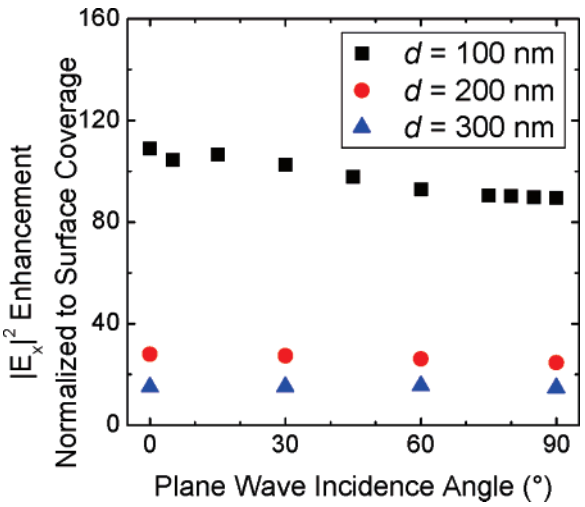

Figure 3. Computed field intensity enhancements in a plane 10 nm below the np-Ag array for different incident plane wave angles, θ, where the angle θ is measured from the particle plane. The pitch is 400 nm, and the np-Ag diameters are 100, 200, and 300 nm (squares, circles, and triangles, respectively).

where the bulk plasmon frequency is $\omega_{b,Ag} = 1.72 \times 10^{16}$ rad s^{-1}, and the plasmon decay rate is $\gamma_{Ag} = 8.35 \times 10^{13}$ rad s^{-1}. It was not possible to simulate an interface that laid along a periodic boundary;[19] therefore, the fused silica ($\epsilon_{SiO_2} = 2.2$) under the nanoparticles and the air ($\epsilon_{air} = 1$) around and above the nanoparticles were represented by a single effective medium that represented the distribution of the electric field above and below the plane of the silica−air interface. This approach was justified by iteratively solving for the distribution until a self-consistent solution was achieved. In this way, 70% of the field emanating from a resonant Ag nanoparticle was found to lie above the interface, and 30% was found to lie in the substrate. The effective medium was thus chosen to have a dielectric constant of $\epsilon_{eff} = (0.3\epsilon_{SiO_2} + 0.7\epsilon_{air}) = 1.36$.

The spectral response of the np-Ag array was determined by illuminating the particle assemblies with a plane wave incident normal to the plane of particles (*y*-axis in Figure 1a). The wave was polarized in the plane of the array (along the *x*-axis), as indicated by the arrow, *P*, in Figure 1b. After 75 fs, the incident plane wave was interrupted, and the electric field distribution was allowed to relax. The ring-down of the field was recorded for 100 fs at specific locations in the array. The inset to Figure 2 presents a characteristic ring-down transient, taken at the center of a nanoparticle in a np-Ag array with $d = 155$ nm, for excitation on resonance at $\lambda = 705$ nm. Figure 2 presents a Fourier transform of this decaying field, which yielded the corresponding plasmon response spectrum, and indicates the presence of a resonance peak at 705 nm.

Spatially resolved images of the electric field distribution around the particles were obtained by illuminating the particles at the resonant frequency determined for the corresponding array, using a plane wave normal to the sample, and allowing the array to store energy for 100 fs. The field distribution was then recorded in a plane 10 nm below the bottom of the np-Ag array, that is, where the emitters were located. This squared field amplitude was integrated over a full optical cycle to provide the time-averaged value of the local-field intensity, and this value was integrated over the plane of the nc-Si emitters to provide a comparison between the simulation output data and the experimental measurements.

Results and Discussion

To verify whether the 20 nm high cylindrical silver nanoparticles (np-Ag) having diameters of 50−300 nm were small enough to justify the reciprocal approach[21] described above, the electric field intensity enhancement was calculated in the nc-Si plane for a range of incident angles. Figure 3 shows the electric field intensity enhancement generated by plane wave illumination as a function of the angle of incidence relative to the *z*-axis (i.e., $\theta = 90°$ for normal incidence) for three representative nanoparticle diameters (100, 200, and 300 nm) calculated at the plasmon resonance frequency for each sample. The incident plane wave is polarized in the *x*-direction (see Figure 1 for axis definition), and therefore, only the *x*-component of the electric field is considered. This is justified by the fact that, since we detect experimentally only light that propagates normal to the plane of the particles, the Si quantum dot emission of interest must originate from in-plane dipoles, which can only couple to the longitudinal modes of the metal nanoparticles. In Figure 3, the largest variation of field enhancement with angle is found for the largest particles, as expected. This variation of 15% thus provides an upper limit to the error in the simulation data shown hereafter. Since this error is small relative to the dynamic range of enhancements in field intensity studied herein, the electric field intensity enhancement, as calculated based on FDTD simulations at a single angle, is an appropriate measure for the radiative decay rate enhancement.

Figure 4 shows the computed plasmon resonance spectra (solid lines) recorded in the center of the metal nanoparticle, as obtained from simulations of arrays having $p = 400$ nm and $d = 260$, 230, 190, 185, 165, and 140 nm, from top to bottom, respectively. Also shown are the measured transmission spectra of representative experimental samples (dashed lines) having the same set of nanoparticle diameters. The calculations reveal a gradual red shift of the resonance spectrum for increasing particle diameter, as has been observed in the transmission spectra. The changes in resonance frequency are dominated by size (and aspect ratio) effects, and the red shift can thus be ascribed to the increased particle diameter, although a secondary contribution is present from the increased interparticle coupling that occurs as particle diameters increase at a fixed pitch.

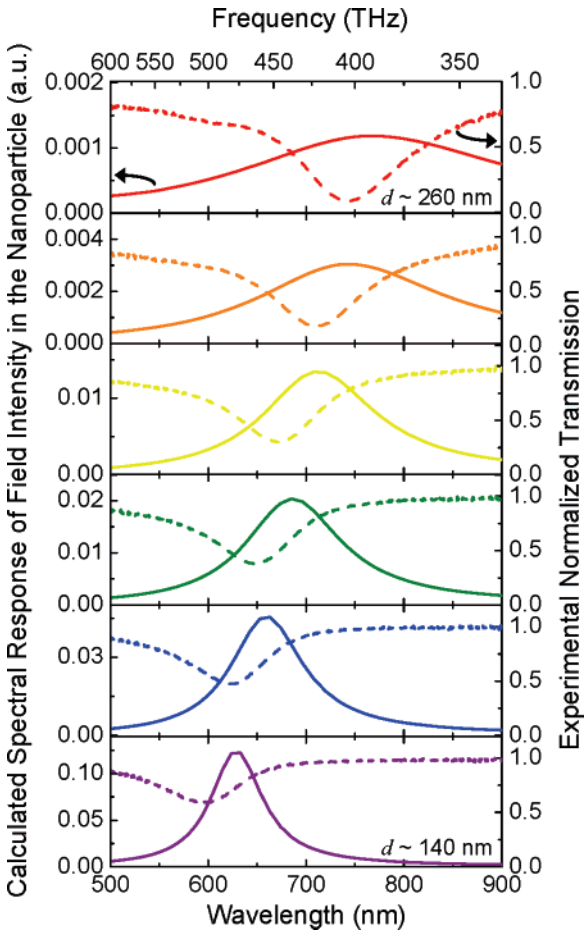

Figure 4. Calculated plasmon resonance spectra (solid lines) and one representative experimental transmission measurement (dashed lines) for np-Au arrays with $d = 260$, 230, 190, 185, 165, and 140 nm (from top to bottom).

Calculations on isolated individual particles (rather than arrays), not shown here, yielded spectra that were blue-shifted by up to 100 nm compared to the spectra calculated for the nanoparticle arrays, verifying that the interaction between particles plays a role in determining the observed response of such arrays.

Sample-to-sample variation causes subtle disagreements between experiment and theory for any single experimental sample. For instance, in Figure 4, the measured transmission peak is consistently blue-shifted relative to the calculated enhancement peak. However, when the transmission measurements are repeated on several experimental samples, these differences vanish, as illustrated in Figure 5. This figure shows the peak wavelength of the calculated resonance spectrum for $p = 400$ nm np-Ag arrays having particle diameters in the 135−320 nm range. Experimentally determined minima of transmission spectra are also shown (averaged over 4−8 samples for each value of d). Within the error bars, which arise from the sample-to-sample variations in experimental measurements, good agreement was observed between the experimental data and the simulations.

The electric field intensity throughout the three-dimensional space about each np-Ag array was also computed numerically. As an example, Figure 1b and c shows the field intensity/amplitude distributions for an array having $d = 135$ nm excited at its computed resonance wavelength of 633 nm. The incident light was polarized in the x-direction. Figure 1b displays the electric field intensity at a cut along a plane through the center of the Ag particles. Figure 1c shows a cut along the plane

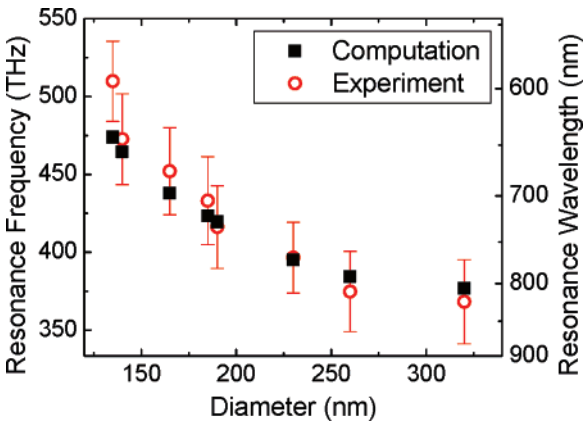

Figure 5. Comparison of resonance wavelengths derived from computations (squares) to those derived from an average over several (3−8) experimental transmission measurements (circles).

parallel to the np-Ag plane at a depth of 10 nm below the base of the nanoparticles, where the nc-Si emitters are located in the experimental samples. In these figures, four subsequent contour lines represent an order of magnitude change in the x-component of the field intensity.

In the experiments of ref 13, the nc-Si were distributed uniformly across a plane. A measure of the field intensity experienced by an average emitter in this plane can be found by integrating the calculated electric field intensities over the area of the plane. For example, the average field intensity felt by a nc-Si emitter in the plane beneath an array of $d = 135$ nm np-Ag was found by integrating the field intensity plotted in Figure 1c over the area of that figure. This intensity was further normalized by the incident field and time-averaged over an optical cycle. According to eq 1, this averaged computed field intensity enhancement should be directly reflected in a PL radiative rate enhancement. In the high pump flux regime in which the experiments were performed,[13] the steady-state PL intensity is directly proportional to the radiative rate of the PL. A measured enhancement of the PL intensity therefore directly reflects an increase in the radiative decay rate, regardless of the existence of nonradiative decay paths. The measured PL intensity enhancement[13] should therefore be equal to the field intensity enhancement computed in the present work.

Figure 6a shows the computed time-averaged field intensity enhancement in the nc-Si plane for arrays having a fixed pitch of 400 nm, with particle diameters ranging from 20 to 320 nm (squares). Two trends are observed in the calculations. First, at small particle diameters, the average enhancement increased with increasing particle diameter. This effect can be ascribed to the increasing np-Ag surface coverage, which reflects the fraction of nc-Si emitters that coupled to the metal nanoparticles (in the limit of infinitesimal metal particle diameter, all nc-Si are uncoupled). The surface coverage effect is removed in Figure 6b, in which the computed and experimental field enhancements are normalized by the np-Ag surface coverage. These data therefore represent the local field enhancement under the nanoparticle. Second, above an optimum diameter of ~100 nm, the average enhancement decreases due to the decreasing local field in the nc-Si plane with increasing particle diameter. This behavior can be attributed to two important effects; (1) in the absence of coupling, the local field enhancement decreases with increasing diameter,[25] and most importantly, (2) as the particles increase in size at a fixed pitch, the interparticle coupling increases, and a proportionally larger part of the plasmon field lies in the lateral gap between the particles, resulting in a

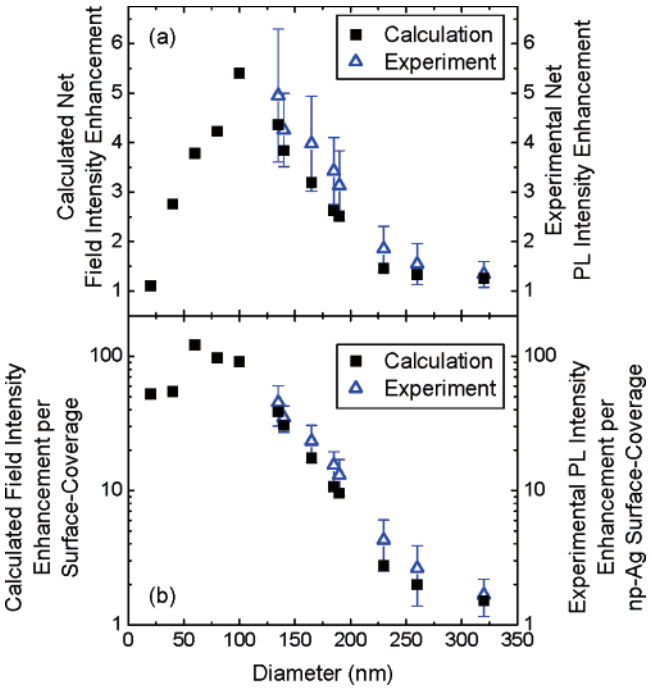

Figure 6. (a) Computed (squares) field intensity enhancement factors for arrays of np-Ag with various diameters and experimentally determined (triangles) PL enhancement factors. (b) Computed and experimental enhancements normalized by the np-Ag surface coverage.

decreased field in the nc-Si plane. Though the present study is limited to examining arrays of np-Ag 20 nm in height, these principles hold true for all sizes and shapes of nanoparticles; the local field enhancement decreases about larger particles, and increased particle−particle coupling draws the field into the interparticle spaces.

Figure 6a also shows the experimentally determined enhancement of the PL intensity of the nc-Si emitters (triangles). Within the error bars, good agreement was observed between experiment and calculations. This agreement indicates that eq 1 accurately describes the phenomenon of plasmon-enhanced photoluminescence in the size regime under investigation. The results depicted in Figure 6 also suggest that an optimum PL enhancement can be found by simultaneously optimizing the field enhancement and the density of the array. Optimization of the PL enhancement thus involves optimization of the metal particle diameter and the array pitch, keeping in mind that the array resonance frequency will shift with such geometrical changes.

A maximum field enhancement in the nc-Si plane cannot be straightforwardly attained by selecting an array with an arbitrarily high density of very small Ag nanoparticles. Figure 7a shows the field enhancement in the plane of the nc-Si at a depth of 10 nm beneath the bottom of an np-Ag array, for np-Ag arrays having $d = 50$ and 100 nm. The smallest pitches were 50 and 100 nm, respectively (i.e., touching cylinders), and the largest pitch was $p = 800$ nm. The results in this figure indicate that, despite the decreasing surface coverage upon increasing particle pitch, the field intensity enhancement in the nc-Si plane increases with increasing pitch until the pitch becomes much larger than the particle diameter. Figure 7b shows this same enhancement normalized for surface coverage. In the size regime considered herein, an increased pitch led to a decrease in the field intensity enhancement per particle as measured in the nc-Si plane, as schematically indicated in the insets to Figure 7. This can again be attributed to the fact that the greater interparticle coupling between more closely spaced (smaller pitch) np-Ag drew the

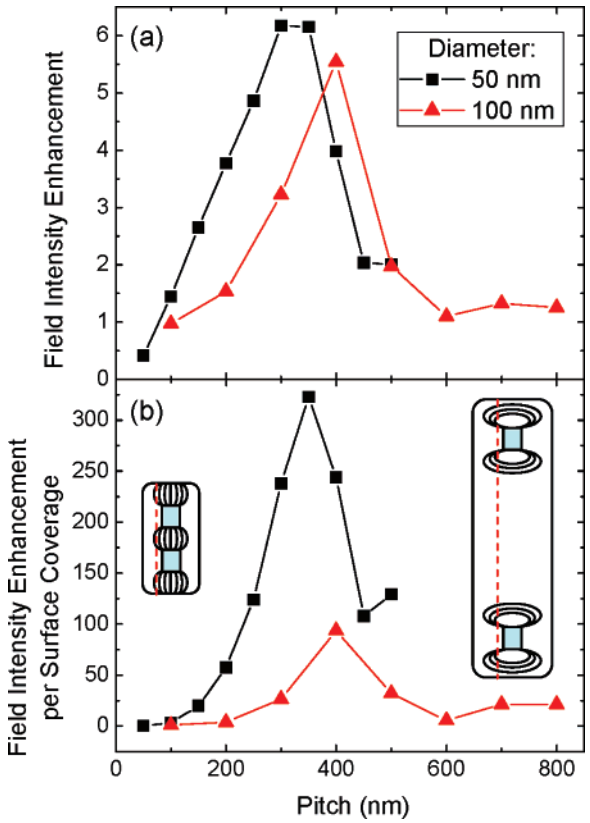

Figure 7. (a) Computed field intensity enhancement in the nc-Si plane for arrays of np-Ag with 50 nm (black squares) and 100 nm (red triangles) diameters and with varying pitches. (b) Computed field enhancements normalized by the np-Ag surface coverage. The insets are schematics illustrating the difference in field distribution between closely coupled particles (left side) and distantly coupled particles (right side), where the blue rectangles are np-Ag, the red dashed line is the nc-Si plane, and the black curves represent the enhanced field intensity, which is drawn into the lateral np-Ag gaps as the interparticle coupling increases.

enhanced field in to the lateral gaps between Ag nanoparticles and out of the nc-Si plane that is 10 nm beneath the np-Ag plane. Similar effects are observed for the 50 and 100 nm diameter particles, with a smaller enhancement and a larger optimum pitch for the 100 nm diameter particles. The largest surface-average field enhancement in the present simulations is a factor 6 for 50 nm diameter particles with a 300−350 nm pitch. Note that the surface coverage for this geometry is only 6%.

Given the constraints of 20 nm thick cylindrical np-Ag particles arranged in a plane above a plane of emitters, further modifications within these constraints, such as replacing the circular np-Ag particles with squares or such as changing the array symmetry from a square to a hexagonal lattice arrangement (data not shown), were found computationally to have no significant effect on the field enhancement in the plane of the nc-Si emitters. The depth dependence of the field intensity under the arrays has also been evaluated through simulations. Figure 8 depicts the integrated field intensity as a function of depth for arrays having $p = 400$ nm and $d = 100$, 135, 185, and 320 nm. For all diameters, in the first 20 nm, the field intensity decreased rapidly with depth. The field enhancement was largest for the smallest particles and extended well beyond 40 nm for these smallest particles. For smaller distances ($\Delta < 5$ nm), quenching to the metal became dominant, and field enhancement calculations alone were not sufficient to determine the PL enhancement.

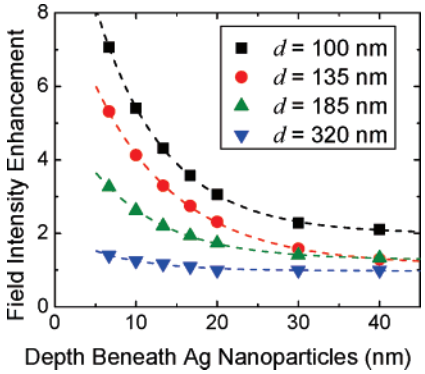

Figure 8. In-plane field intensity enhancement as a function of depth from the base of the np-Ag array for various np-Ag diameters, *d*.

Simulations of this type can clearly be used to design future experiments and to predict the resonance frequency of a nanoparticle array a priori. This parameter could be important when coupling metals to emitters having sharp emission spectra, such as dyes and direct-band-gap semiconductor materials. In such situations, resonant coupling could only occur if the metal array was carefully designed to have a plasmon resonance spectrum that overlapped the precise emission spectrum. The simulations also provide beneficial three-dimensional maps which suggest the ideal placement of emitters near metals in different arrangements than that of the coplanar geometry considered in this paper. The numerical studies described herein provide information about the far-field emission enhancement that results from near-field interactions. However, the results also provide insight into the local-field intensity as a function of position on a scale smaller than that which can be measured with far-field optics.

Conclusions

Electromagnetic simulations of the resonance spectra and field intensity distributions around Ag nanoparticles were performed with the aim to study plasmon-enhanced luminescence near arrays of these particles. The simulations focused on determining the field enhancement in a plane at a fixed depth of 10 nm below the metal nanoparticles in order to enable comparison with experiments. Simulations showed a red shift of the plasmon resonance from 600 to 800 nm for particle sizes increasing from 140 to 340 nm, in good agreement with experiments. For a typical array pitch of 400 nm, simulations showed that interparticle coupling red shifted the resonance frequencies. In the 150−300 nm particle diameter range, experimental and calculated luminescence enhancements were in good agreement. The largest field enhancements were found for particles with diameters of 50 nm. At small interparticle spacing, a significant fraction of the field is drawn into the space between the metal particles. As a result, the largest surface-averaged field enhancement was observed for 50 nm diameter particles at a pitch of 300−350 nm, that is, a surface coverage of only 6%. The calculations provide fundamental insights into the factors that determine plasmon-enhanced emission in coupled nanoparticle arrays and can be used to study a wide range of alternative geometries.

Acknowledgment. This work was partially supported by NSF Grant No. CHE-0604894 and by AFOSR MURI Award No. FA9550-04-1-0434. Work at AMOLF is part of the research program of FOM, supported by NWO and NANONED, a nanotechnology program of the Dutch Ministry of Economic Affairs. Metal nanoparticle arrays were fabricated and analyzed using the facilities of the Amsterdam nanoCenter.

References and Notes

(1) Min, K. S.; Shcheglov, K. V.; Yang, C. M.; Atwater, H. A.; Brongersma, M. L.; Polman, A. *Appl. Phys. Lett.* **1996**, *69*, 2033.
(2) Brongersma, M. L.; Polman, A.; Min, K. S.; Boer, E.; Tambo, T.; Atwater, H. A. *Appl. Phys. Lett.* **1998**, *72*, 2577.
(3) Fischer, T.; Petrova-Koch, V.; Shcheglov, K.; Brandt, M. S.; Koch, F. *Thin Solid Films* **1996**, *276*, 100.
(4) Gersten, J.; Nitzan, A. *J. Chem. Phys.* **1981**, *75*, 1139.
(5) Wokaun, A.; Lutz, H. P.; King, A. P.; Wild, U. P.; Ernst, R. R. *J. Chem. Phys.* **1983**, *79*, 509.
(6) Kümmerlen, J.; Leitner, A.; Brunner, H.; Aussenegg, F. R.; Wokaun, A. *Mol. Phys.* **1993**, *80*, 1031.
(7) Shimizu, K. T.; Woo, W. K.; Fisher, B. R.; Eisler, H. J.; Bawendi, M. G. *Phys. Rev. Lett.* **2002**, *89*, 117401.
(8) Kulakovich, O.; Strekal, N.; Yaroshevich, A.; Maskevich, S.; Gaponenko, S.; Nabiev, I.; Woggon, U.; Artemyev, M. *Nano Lett.* **2002**, *2*, 1449.
(9) Anger, P.; Bharadwaj, P.; Novotny, L. *Phys. Rev. Lett.* **2006**, *96*, 113002.
(10) Kühn, S.; Håkanson, U.; Rogobetem, L.; Sandoghdar, V. *Phys. Rev. Lett.* **2006**, *97*, 017402.
(11) Biteen, J. S.; Pacifici, D.; Lewis, N. S.; Atwater, H. A. *Nano Lett.* **2005**, *5*, 1768.
(12) Mertens, H.; Polman, A.; Biteen, J. S.; Atwater, H. A. *Nano Lett.* **2006**, *6*, 2622.
(13) Biteen, J. S.; Lewis, N. S.; Atwater, H. A.; Mertens, H.; Polman, A. *Appl. Phys. Lett.* **2006**, *88*, 131109.
(14) Mertens, H.; Koenderink, A. F.; Polman, A. *Phys. Rev. B* **2007**, *75*, accepted.
(15) Khlebtsov, B.; Melnikov, A.; Zharov, V.; Khlebtsov, N. *Nanotechnology* **2006**, *17*, 1437.
(16) Kelly, K. L.; Coronado, E.; Zhao, L. L.; Schatz, G. C. *J. Phys. Chem. B* **2003**, *107*, 668.
(17) Zhao, L. L.; Kelly, K. L.; Schatz, G. C. *J. Phys. Chem. B* **2003**, *107*, 7343.
(18) Haynes, C. L.; McFarland, A. D.; Zhao, L. L.; Van Duyne, R. P.; Schatz, G. C.; Gunnarsson, L.; Prikulis, J.; Kasemo, B.; Kall, M. *J. Phys. Chem. B* **2003**, *107*, 7337.
(19) *Maxwell's Equations by Finite Integration Algorithm (MaFIA)*, 4th ed.; Gesellschaft für Computer-Simulationstechnik (CST): Darmstadt, Germany, 2000.
(20) Ruppin, R. *J. Chem. Phys.* **1982**, *76*, 1681.
(21) Hill, S. C.; Videen, G.; Pendleton, J. D. *J. Opt. Soc. Am. B* **1997**, *14*, 2522.
(22) Bohren, C. F.; Huffman, D. R. *Absorption and Scattering of Light by Small Particles*; John Wiley & Sons, Inc.: New York, 1983.
(23) Sweatlock, L. A.; Maier, S. A.; Atwater, H. A.; Penninkhof, J. J.; Polman, A. *Phys. Rev. B* **2005**, *71*, 235408.
(24) Palik, E. D. *Handbook of Optical Constants*; Academic Press: London, 1985.
(25) Wokaun, A.; Gordon, J. P.; Liao, P. F. *Phys. Rev. Lett.* **1982**, *48*, 957.